

Electronic structure and x-ray magnetic circular dichroism in $A_2CrB'O_6$ ($A = Ca, Sr; B' = W, Re, \text{ and } Os$) oxides

V.N. Antonov and L.V. Bekenov

*G.V. Kurdyumov Institute for Metal Physics of the NAS of Ukraine
36 Academician Vernadsky Boulevard, Kiev 03142, Ukraine
E-mail: antonov@imp.kiev.ua*

Received August 17, 2016, published online March 24, 2017

A systematic electronic structure study of $A_2CrB'O_6$ ($A = Ca, Sr; B' = W, Re, \text{ and } Os$) has been performed by employing the local spin-density approximation (LSDA) as well as the GGA and LSDA+ U methods using the fully relativistic spin-polarized Dirac linear muffin-tin orbital band-structure method. We investigated the effects of the subtle interplay among the spin-orbit coupling, electron correlations, and lattice distortion on the electronic structure of the double perovskites. First principles calculations predict that Sr_2CrOsO_6 is (before considering spin-orbit coupling) actually a ferrimagnetic semimetal with precisely compensating spin moments, or spin-asymmetric compensated semimetallic ferrimagnet in which the electrons and holes are each fully polarized and have opposite spin directions, in spite of a zero net moment and hence no macroscopic magnetic field. Spin-orbit coupling degrades this by giving a nonzero total moment, but the band structure is little changed. Therefore, the observed saturation moment of ferrimagnetic Sr_2CrOsO_6 is entirely due to spin-orbit coupling. The x-ray absorption spectra and x-ray magnetic circular dichroism at the W, Re, Os, and Cr $L_{2,3}$, and Cr and O K edges were investigated theoretically from first principles. A qualitative explanation of the XMCD spectra shape is provided by the analysis of the corresponding selection rules, orbital character and occupation numbers of individual orbitals. The calculated results are in good agreement with experimental data. The complex fine structure of the Cr $L_{2,3}$ XAS in Sr_2CrWO_6 and Sr_2CrReO_6 was found to be not compatible with a pure Cr^{3+} valency state. The interpretation demands mixed valent states. We found that possible oxygen vacancies lead to a mixed valency at the Cr site, double peak structure at the Cr $L_{2,3}$ edges and reduce the saturation magnetization in Sr_2CrWO_6 and Sr_2CrReO_6 .

PACS: 75.50.Cc Other ferromagnetic metals and alloys;
71.20.Lp Intermetallic compounds;
71.15.Rf Relativistic effects.

Keywords: electronic structure, x-ray absorption, x-ray circular dichroism, first principles calculations.

1. Introduction

Double perovskites (DP) $A_2BB'O_6$ ($A =$ alkaline earth or rare earth and BB' are heterovalent transition metals such as $B = Fe, Cr, Mn, Co, Ni; B' = Mo, W, Re, Os$) was established as new colossal magneto-resistance (CMR) materials at low magnetic field and room temperature [1,2]. They often demonstrate intrinsically complex magnetic structures and a wide variety of physical properties as a consequence of the strong interplay between structure, charge and spin ordering [3] (see Ref. 4 for a review article on these materials). The fact that the DP seem to be ferromagnetic metals with high Curie temperatures T_C and apparently have highly spin polarized conduction band makes these materials interesting for applications in spintronic

devices such as magnetic tunnel junctions or low-field magnetoresistive sensors [1,4,5]. However, the DP are also of fundamental interest since both their basic physics and materials aspects are not well understood.

The series $A_2CrB'O_6$ ($A = Ca, Sr$) with B' being W, Re, and Os ions is very promising due to their record high values of T_C . Originally reported 44 years ago by Sleight *et al.* [6], the compound Sr_2CrOsO_6 has been revisited by Kronenberger *et al.* [7]. The motivation was that this member follows a series of half-metals $Sr_2CrB'O_6$, $B' = W, Re$, with very high magnetic ordering temperatures ($T_C = 500$ and 635 K, respectively) [8,9]. The compound Sr_2CrOsO_6 is special, as it has a completely filled $5d t_{2g}$ minority-spin orbital, while the majority-spin channel is still gaped. Sr_2CrOsO_6 has an even higher ordering temperature $T_C = 725$ K [7],

the highest known in this class, and was reported to be insulating. Besides record high Curie temperatures $A_2CrB'O_6$ DP show other interesting physical properties, such as, substantially large Kerr rotations [10] of about -2° to -2.5° for Sr_2CrWO_6 and Sr_2CrReO_6 , a moderately large Faraday rotation of about $-0.25 \cdot 10^6$ deg/cm in insulating Sr_2CrOsO_6 and relatively large magnetic coercivity and magneto-crystalline anisotropy energies ($MAE = E_{001} - E_{111} = 0.38$ meV) in Sr_2CrReO_6 [11]. The former is unexpected considering the octahedral coordination and nearly cubic local environments in Sr_2CrReO_6 .

Despite of many experimental and theoretical researches of the electronic and magnetic structures of $A_2CrB'O_6$ compounds, some controversies still remain from both the theoretical and the experimental point of views. From the theoretical side despite several important density functional theory (DFT) calculations of Sr_2CrOsO_6 [7,12–14], it is still no clear why Sr_2CrOsO_6 is an insulator. It is not a band insulator, since the bands are partially filled. It is not a Slater insulator, given the large moment observed on Cr. It is not a priori clear how it can be a Mott insulator either, given the weak correlations on Os relative to the large bandwidth of $5d$ orbitals. Why is there a net moment, given that both Cr and Os are in d^3 configurations? The role of spin-orbit coupling (SOC) on Os should be significant: DFT calculations show zero net moment in the spin-polarized calculations [14], but a net moment is appeared when SOC is included [12,14]. On the other hand, x-ray magnetic circular dichroism experiments [7] show insignificant Os orbital moment.

From the experimental point of view some papers on the basis of the measured electric, thermal, optical, and magnetic properties suggested that Sr_2CrReO_6 could be a metallic ferromagnet with $T_C = 635$ K [2,15]. Theoretical calculations support this observation producing a half-metallic band structure in Sr_2CrReO_6 [10,11,16,17]. However, Hauser et al. [18] report growth of Sr_2CrReO_6 epitaxial films with 99% Cr/Re ordering and crystalline perfection comparable to those of high-quality semiconductor films. The samples show a smaller Curie temperature of 508 K and a saturation magnetization of $1.29 \mu_B$ per formula unit. Unexpectedly, electrical transport and optical absorption measurements indicate that Sr_2CrReO_6 epitaxial film might be a semiconductor with a band gap of 0.21 eV.

The x-ray absorption spectroscopy (XAS) and x-ray magnetic circular dichroism (XMCD) measurements in these compounds were carried out by several authors [7,19–22]. Majewski et al. [20] investigated the magnetic moment of the W ion in the ferrimagnetic double perovskites Sr_2CrWO_6 and Ca_2CrWO_6 by x-ray magnetic circular dichroism at the W $L_{2,3}$ edges. In both compounds a finite negative spin and positive orbital magnetic moments were detected. The same authors [21] provide a similar investigation measuring Re $5d$ spin and orbital magnetic moments in the ferrimagnetic double perovskite Sr_2CrReO_6 by x-ray mag-

netic circular dichroism at the Re $L_{2,3}$ edges. A large $5d$ spin magnetic moment of $-0.68 \mu_B$ and a considerable orbital moment of $+0.25 \mu_B$ have been detected. Krockenberger et al. [7] provide band-structure calculations for Sr_2CrOsO_6 using the generalized gradient approximation including spin-orbit coupling (GGA+SO) and measured XAS and XMCD spectra at the Os $L_{2,3}$ edges in Sr_2CrOsO_6 . They found significant discrepancy between theoretically calculated and experimentally estimated spin and magnetic moments at the Os site. However, the theoretical spin magnetic moment at the Cr site was in good agreement with neutron measurements.

The aim of this work is the detailed theoretical investigations of the electronic structure and x-ray magnetic circular dichroism in $A_2CrB'O_6$ ($A = Ca$ and $Sr; B' = W, Re, \text{ and } Os$) DP. Although a few DFT based studies [7,8,10–14,16,17,23] exist for some of these compounds, to the best of our knowledge, no comprehensive theoretical study exists to address the origin of the x-ray magnetic dichroism in the series. The energy band structure of $A_2CrB'O_6$ compounds in this paper is calculated within the *ab initio* approach taking into account strong electron correlations by applying a local spin-density approximation to the density functional theory supplemented by a Hubbard U term [24].

The paper is organized as follows. The computational details are presented in Sec. 2. Section 3 presents the electronic structure of $A_2CrB'O_6$ compounds. Section 4 presents the XAS and XMCD spectra of $A_2CrB'O_6$ compounds. Theoretical results are compared to experimental measurements. Finally, the results are summarized in Section 5.

2. Computational details

2.1. Crystal structure

Double ordered perovskites ($A_2BB'O_6$) possess a modified perovskite structure (ABO_3) where the BO_6 and $B'O_6$ octahedra are alternatively arranged in two fcc sublattices. The A sites are occupied by alkaline or rare-earth ions, while the B and B' sites correspond to transition metal ions. This cubic structure can be well described within the $Fm\bar{3}m$ space group. However, this structure is very often distorted as a consequence of the pressure or temperature variations.

At room temperature the crystal structure is cubic ($Fm\bar{3}m$; group number 225) for Sr_2CrWO_6 , tetragonal ($I4/m$; group number 87) for Sr_2CrReO_6 , and monoclinic ($P2_1/n$; group number 14) for Ca_2CrWO_6 [4] (see Fig. 1). The oxygen atoms surrounding the Cr and B' sites provide the octahedral environment. The structural differences can be understood taking into account the tilting of the Cr/B'–O octahedra. While the A cation size is getting smaller, empty space shows up around it and needs to be filled up. The cubic structure is then replaced by the space groups exhibiting lower symmetry. Using Glazer's terminology [25]

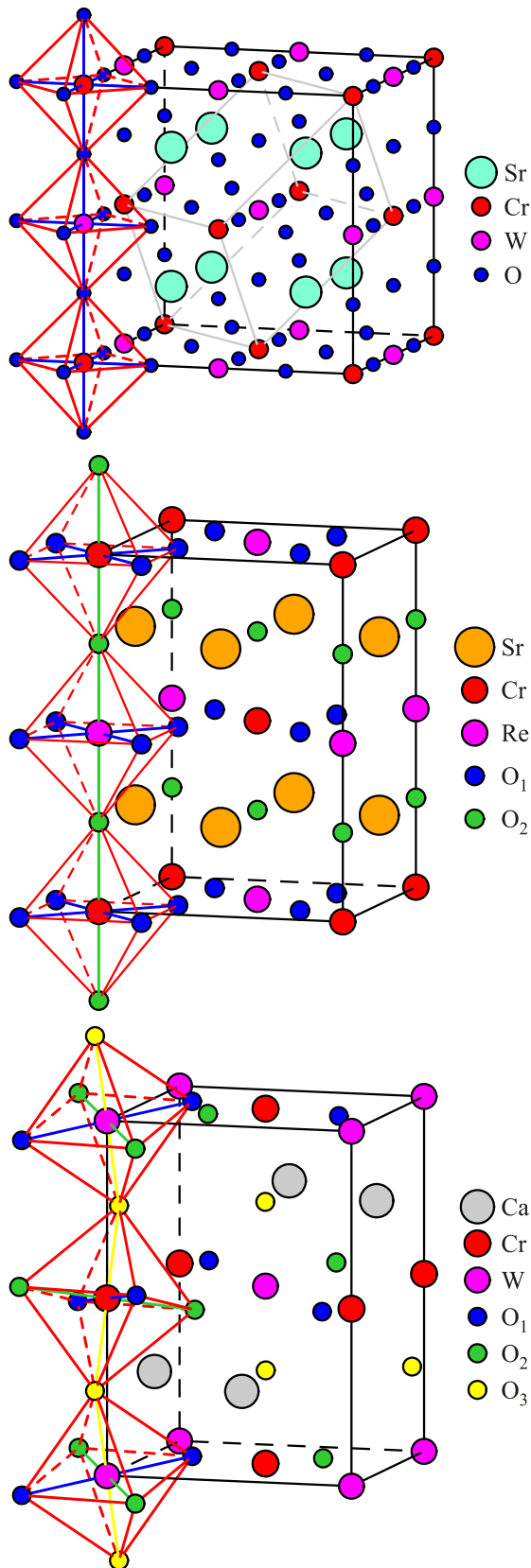


Fig. 1. (Color online) Upper panel: schematic representation of $Fm\bar{3}m$ Sr_2CrWO_6 structure (gray lines show the primitive cell). Middle panel: schematic representation of $I4/m$ $\text{Sr}_2\text{CrReO}_6$ structure. Lower panel: the primitive cell of $P2_1/n$ Ca_2CrWO_6 structure.

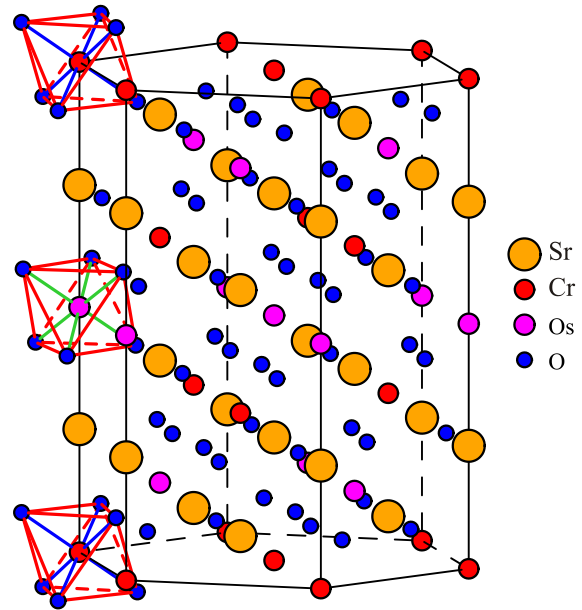


Fig. 2. (Color online) schematic representation of rhombohedral $R\bar{3}$ $\text{Sr}_2\text{CrOsO}_6$ structure.

the $a^0a^0c^-$ octahedral tilt is responsible for the occurrence of the $I4/m$ space group, while the $P2_1/n$ space group arises from the $a^+b^-b^-$ tilt [26]. Basically, two different types of distortion are included in the monoclinic $P2_1/n$ structure of Ca_2CrWO_6 oxide shown in lower panel of Fig. 1. One is a rotating the CrO_6 and WO_6 octahedra around the c axis and tilting them in alternating directions around the b axis so that the Cr-O-W angle changes from 180° (GdFeO_3 -type distortion). The second type of crystal distortion in Ca_2CrWO_6 is the Jan-Teller distortion caused the deformation of the CrO_6 and WO_6 octahedra, thus creating different Cr(W)-O bond lengths.

The low (2 K) temperature phase of $\text{Sr}_2\text{CrOsO}_6$ is a rhombohedral double perovskite structure with space group $R\bar{3}$ (Fig. 2), and returns to the cubic double perovskite structure ($Fm\bar{3}m$) at higher temperatures (500 K) [7].

2.2. X-ray magnetic circular dichroism

Magneto-optical (MO) effects refer to various changes in the polarization state of light upon interaction with materials possessing a net magnetic moment, including rotation of the plane of linearly polarized light (Faraday, Kerr rotation), and the complementary differential absorption of left and right circularly polarized light (circular dichroism). In the near visible spectral range these effects result from excitation of electrons in the conduction band. Near x-ray absorption edges, or resonances, magneto-optical effects can be enhanced by transitions from well-defined atomic core levels to transition symmetry selected valence states.

Within the one-particle approximation, the absorption coefficient $\mu_j^\lambda(\omega)$ for incident x ray of polarization λ and photon energy $\hbar\omega$ can be determined as the probability of

electronic transitions from initial core states with the total angular momentum j to final unoccupied Bloch states

$$\mu_{\lambda}^j(\omega) = \sum_{m_j} \sum_{n\mathbf{k}} |\langle \Psi_{n\mathbf{k}} | \Pi_{\lambda} | \Psi_{jm_j} \rangle|^2 \delta(E_{n\mathbf{k}} - E_{jm_j} - \hbar\omega) \times \theta(E_{n\mathbf{k}} - E_F), \quad (1)$$

where Ψ_{jm_j} and E_{jm_j} are the wave function and the energy of a core state with the projection of the total angular momentum m_j ; $\Psi_{n\mathbf{k}}$ and $E_{n\mathbf{k}}$ are the wave function and the energy of a valence state in the n th band with the wave vector \mathbf{k} ; E_F is the Fermi energy.

Π_{λ} is the electron-photon interaction operator in the dipole approximation

$$\Pi_{\lambda} = -e\mathbf{a}\mathbf{a}_{\lambda}, \quad (2)$$

where \mathbf{a} are the Dirac matrices, \mathbf{a}_{λ} is the λ polarization unit vector of the photon vector potential, with $a_{\pm} = 1/\sqrt{2}(1, \pm i, 0)$, $a_{\parallel} = (0, 0, 1)$. Here, + and - denotes, respectively, left and right circular photon polarizations with respect to the magnetization direction in the solid. Then, x-ray magnetic circular and linear dichroisms are given by $\mu_+ - \mu_-$ and $\mu_{\parallel} - (\mu_+ + \mu_-)/2$, respectively. More detailed expressions of the matrix elements in the electric dipole approximation may be found in Refs. 27–30. Matrix elements due to the magnetic dipole and electric quadrupole corrections are presented in Ref. 30.

Concurrent with the development of the x-ray magnetic circular dichroism experiment, some important magneto-optical sum rules have been derived [31–34].

For the $L_{2,3}$ edges the l_z sum rule can be written as [29]

$$\langle l_z \rangle = n_h \frac{4 \int_{L_3+L_2} d\omega(\mu_+ - \mu_-)}{3 \int_{L_3+L_2} d\omega(\mu_+ + \mu_-)}, \quad (3)$$

where n_h is the number of holes in the d band $n_h = 10 - n_d$, $\langle l_z \rangle$ is the average of the magnetic quantum number of the orbital angular momentum. The integration is taken over the whole $2p$ absorption region. The s_z sum rule can be written as

$$\begin{aligned} \langle s_z \rangle + \frac{7}{2} \langle t_z \rangle &= \\ &= n_h \frac{\int_{L_3} d\omega(\mu_+ - \mu_-) - 2 \int_{L_2} d\omega(\mu_+ - \mu_-)}{\int_{L_3+L_2} d\omega(\mu_+ + \mu_-)}, \end{aligned} \quad (4)$$

where t_z is the z component of the magnetic dipole operator $\mathbf{t} = \mathbf{s} - 3\mathbf{r}(\mathbf{r} \cdot \mathbf{s})/|\mathbf{r}|^2$ which accounts for the asphericity of the spin moment. The integration $\int_{L_3} \left(\int_{L_2} \right)$ is taken only over the $2p_{3/2}$ ($2p_{1/2}$) absorption region.

2.3. Calculation details

The details of the computational method are described in our previous papers [35–37], and here we only mention some aspects specific to the present calculations. The calculations presented in this work were performed using the spin-polarized fully relativistic linear-muffin-tin-orbital (LMTO) method [38–40] for the experimentally observed lattice constants [41]. The LSDA part of the calculations was based on the spin-density functional with the Perdew–Wang [42] exchange-correlation potential. The exchange-correlation functional of a GGA-type was also used in the version of Perdew, Burke and Ernzerhof [43,44]. The basis consisted of the s , p , and d LMTO's for Ca, Sr, and O sites and the s , p , d , and f LMTO's for W, Re, and Os sites. The \mathbf{k} -space integrations were performed with the improved tetrahedron method [45] and the self-consistent charge density was obtained with 518, 413, 641, and 980 irreducible \mathbf{k} -points in Ca_2CrWO_6 , Sr_2CrWO_6 , Sr_2CrReO_6 , and Sr_2CrOsO_6 compounds, respectively.

The x-ray absorption and dichroism spectra were calculated taking into account the exchange splitting of core levels. The finite lifetime of a core hole was accounted for by folding the spectra with a Lorentzian. The widths of core level spectra Γ_{L_2} , Γ_{L_3} and K for Cr, W, Re, Os, and O were taken from Ref. 46. The finite apparatus resolution of the spectrometer was accounted for by a Gaussian of width 0.6 eV.

It is well known that the LSDA fails to describe the electronic structure and properties of the systems in which the interaction among the electrons is strong. More advanced methods of electronic structure determination such as LSDA plus self-interaction corrections [47], the LSDA+ U method [24], GW approximation [48], and dynamical mean-field theory [49–51] have sought to remedy this problem and have shown considerable success. Among them, the LSDA+ U method is the simplest and most frequently used. We used the “relativistic” generalization of the rotationally invariant version of LSDA+ U method [52] which takes into account SOC so that the occupation matrix of localized electrons becomes nondiagonal in spin indexes. This method is described in detail in our previous paper [52] including the procedure to calculate the screened Coulomb U and exchange J integrals, as well as the Slater integrals F^2 , F^4 , and F^6 .

The screened Coulomb U and exchange J integrals enter the LSDA+ U energy functional as external parameters and have to be determined independently. These parameters can be determined from supercell LSDA calculations using Slater's transition state technique [53,54], from constrained LSDA calculations (cLSDA) [54–58] or the constrained random-phase approximation (cRPA) scheme [59]. Subsequently, a combined cLSDA and cRPA method was also proposed [60]. The cRPA method, however, is known to yield values of U that are too small in some cases [61].

On the other hand, the cLSDA method produces too large values of U [62]. Therefore, in our calculations we treated the Hubbard U as an external parameter and varied it from 2 to 6 eV. We adjusted the value of U to achieve the best agreement with the experimental spectra. The cLSDA calculations produce $J = 0.9, 0.8,$ and 0.75 eV for W, Re, and Os sites, respectively, in $A_2CrB'O_6$. In the case of $U_{\text{eff}} = U - J = 0$ the effect of the LSDA+ U comes from nonspherical terms which are determined by F^2 and F^4 Slater integrals. This approach is similar to the orbital polarization corrections [29,63–66]. For the LSDA+ U approach with $U = J, U_{\text{eff}} = U - J = 0$ eV we use the notation LSDA+OP throughout the paper.

3. Electronic structure

3.1. Energy bands

Generally in $3d$ transition metal oxides (TMOs), the SOC is typically less than 0.05 eV. This is much smaller than the other important energies in $3d$ TMOs, such as on-site Coulomb interaction energy, U (3–5 eV), and the crystal-field splitting energy, Δ (2–3 eV). Therefore the SOC is not dominant in determining the physical properties of $3d$ TMOs. On the other hand, in the $5d$ TMOs, the SOC is approximately 0.3–0.5 eV [67], and therefore should be taken into account when describing the electronic structure of $5d$ TMOs [68].

3.1.1. Sr_2CrWO_6 and Sr_2CrReO_6

We start with a review of the basic electronic and magnetic properties of the compounds using the standard LSDA and GGA approximations. Figure 3 presents the energy band structures of Sr_2CrWO_6 and Sr_2CrReO_6 calculated in the GGA spin-polarized approximation.

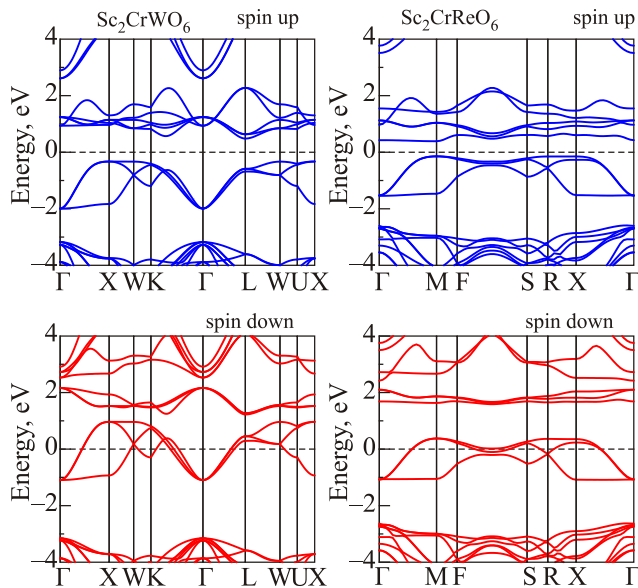


Fig. 3. (Color online) The energy band structure of Sr_2CrWO_6 and Sr_2CrReO_6 calculated in the GGA spin-polarized approximation.

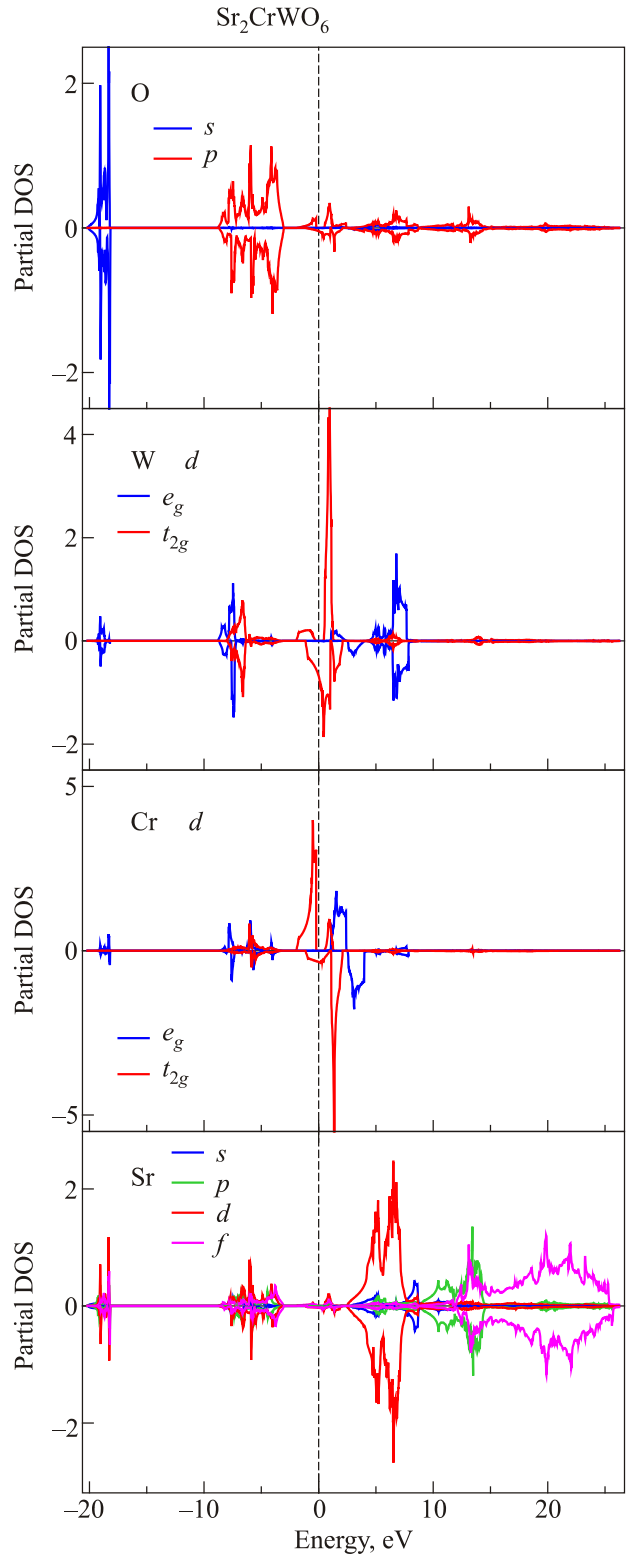


Fig. 4. (Color online) The partial DOSs [in states/(atom-eV)] of Sr_2CrWO_6 calculated in the GGA spin-polarized approximation.

culated in the GGA approach (the LSDA approach produces similar results). The GGA approach gives half-metallic states in Sr_2CrWO_6 and Sr_2CrReO_6 where the only contribution around the Fermi level comes from the minority spins. There is an energy gap of 0.20 eV between the Cr e_g and Re t_{2g} states in the spin-up channel. The total spin

magnetic moment is equal to $3 \mu_B$ in spin-polarized calculations (without taking into account the SOC), which is consistent with the expected half-metallic nature of this compound. A similar conclusion was derived in previous theoretical calculations [10–12,16,17,23,69,70].

The spin-resolved DOSs are presented in Fig. 4. For the Sr_2CrWO_6 , the electronic energy bands between -20.0 and -18.3 eV are dominated by O $2s$ states. O $2p$ states are in the -8.8 to -3.0 eV energy interval. Sr empty $5d$ states occupy the energy interval from 2.5 to 8 eV above the Fermi level. Sr $5p$ states are located from 9 up to 15 eV. Sr $4f$ states are situated at higher energy from 12 to 27 eV. The Fermi energy falls in an energy gap of about 0.7 eV in the majority spin channel, between the fully filled Cr t_{2g} and empty Re t_{2g} bands. Thus, the GGA calculation produces in Sr_2CrWO_6 a half-metallic ferrimagnet.

3.1.2. Sr_2CrOsO_6

Our band structure calculations are based on both cubic ($Fm\bar{3}m$, above 500 K) and rhombohedral ($R\bar{3}$, at 2 K) structures. In the distorted structure, the change in volume is less than 1%, and O and Sr atoms are displaced by 0.015

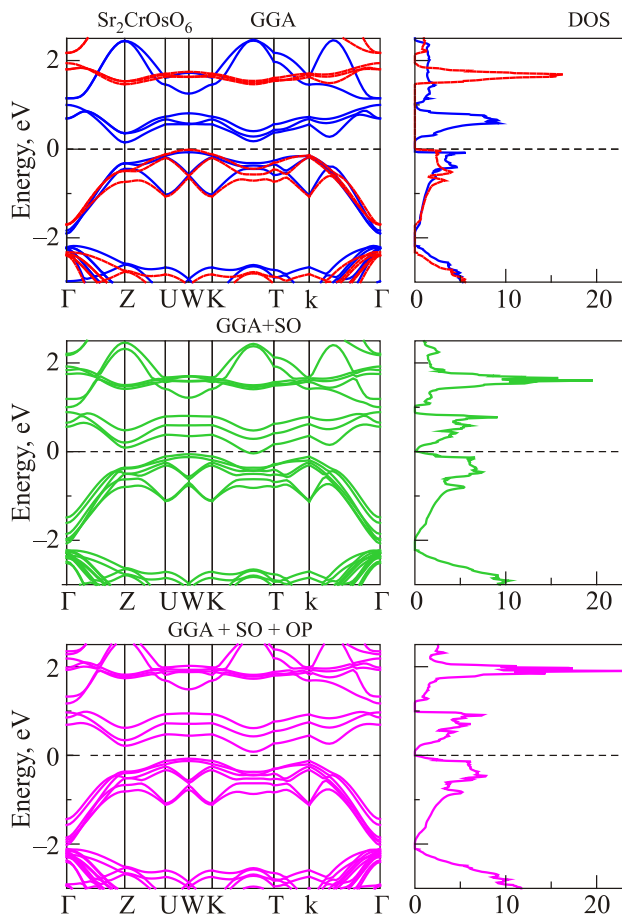


Fig. 5. (Color online) The energy band structure of Sr_2CrOsO_6 for the rhombohedral ($R\bar{3}$) structure calculated in the GGA (upper panel: blue and red lines for the majority and minority channels, respectively), GGA+SO (middle panel), and GGA+SO+OP (lower panel) approximations.

and 0.006 Å, respectively. For Sr_2CrOsO_6 , we found that the $R\bar{3}$ distortion is energetically favored over the cubic structure by 145 meV, in agreement with observation. The distortions due to a size mismatch in the compound have negligible effect on the electronic structure, consistent with the fact that the ions have a filled t_{2g} shell so that the band structure energy is not gained by the distortion.

Figure 5 presents the energy band structure of Sr_2CrOsO_6 for the rhombohedral ($R\bar{3}$) structure calculated in the GGA, GGA with SO included (GGA+SO), and the GGA+SO with orbital polarization correction (GGA+SO+OP) approximations. The partial DOSs for Sr_2CrOsO_6 in the GGA+SO+OP are presented in Fig. 6. The GGA band structure near E_F (without SO correction) of Sr_2CrOsO_6

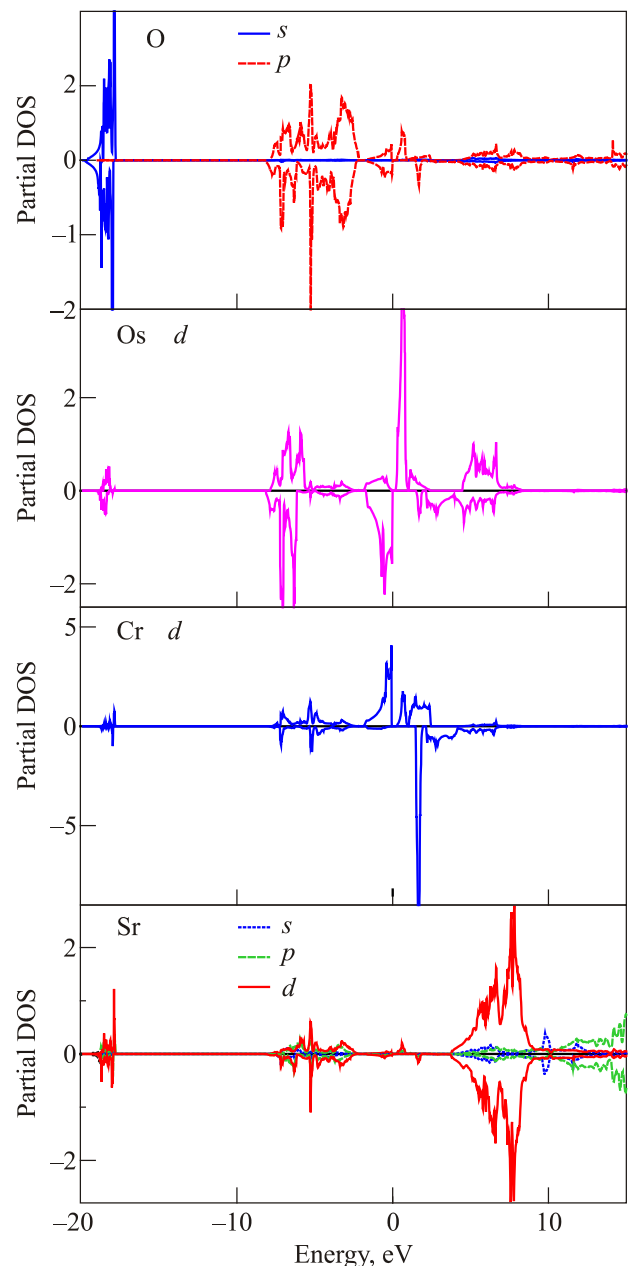


Fig. 6. (Color online) The partial DOSs [in states/(atom·eV)] of Sr_2CrOsO_6 calculated in the GGA+SO+OP approximation.

(upper panel of Fig. 5) agrees well with that of Kronkenberger *et al.* [7] and Lee and Pickett [14]. The fully occupied Os spin-down states and Cr spin-up majority t_{2g} manifolds each have identical width of 1.8 eV. A larger transition metal–O hybridization for a $5d$ ion compared to that of a $3d$ ion reduces the Os spin moment from $3 \mu_B$ by almost a factor of 2, even though both Cr and Os ions have occupied t_{2g} states corresponding to $S = 3/2$. Each spin channel separately has a gap, 0.4 eV for the spin up and 1 eV for spin down, between the Cr and Os t_{2g} manifolds. The majority and minority states show different hybridizations, resulting in differing crystal (ligand) field and exchange splittings on Cr and Os. The crystal field splittings Δ_{cf} are (roughly) as follows: Cr, majority 2.5 eV, minority 1 eV; Os: 2.5 eV for both directions. The exchange splitting in the Os ion (just over 1 eV) is half of that of Cr ion. The distinguishing feature of $\text{Sr}_2\text{CrOsO}_6$ is that the Os t_{2g} bandwidth is equal to its exchange splitting, such that a zero gap lies “between” the corresponding up and down bands. The Cr spin moment of $2.284 \mu_B$ is completely compensated with the Os spin moment of $-1.645 \mu_B$, six O moments of $-0.567 \mu_B$ and two Sr spin moments of $-0.072 \mu_B$. Therefore first principles calculations predict that $\text{Sr}_2\text{CrOsO}_6$ is (before considering SOC) actually a ferrimagnetic semimetal with precisely compensating spin moments, or a spin-asymmetric compensated semimetallic ferrimagnet in which the electrons and holes are each fully polarized and have opposite spin directions, in spite of a zero net moment and hence no macroscopic magnetic field [14]. This is a peculiar state indeed. The SOC degrades this by giving a nonzero total moment, but the band structure is little changed. Upon including the SOC, the Cr moment (with its small SOC) is almost unchanged ($2.289 \mu_B$). The effect on Os is substantial; however, due to mixing with states of the opposite spin, the spin moment is reduced by $0.211 \mu_B$ and an orbital moment of $-0.104 \mu_B$ is induced. The total net moment, $0.545 \mu_B$ reflecting both spin and orbital compensations, is reasonably close to the measured saturation moment of $0.75 \mu_B$ [7] and to the neutron diffraction measurements ($0.73 \mu_B$ at low temperature). (The unusual temperature dependence indicates non-standard behavior of the magnetism in $\text{Sr}_2\text{CrOsO}_6$, so it may be premature to expect close agreement [14].) We can conclude that the observed saturation moment of ferrimagnetic $\text{Sr}_2\text{CrOsO}_6$ is entirely due to the spin-orbit coupling, and without this coupling $\text{Sr}_2\text{CrOsO}_6$ would be spin compensated (zero net moment). A similar conclusion was also drawn by Lee and Pickett [14].

The band structure of $\text{Sr}_2\text{CrOsO}_6$ with the spin-orbit coupling in the GGA+SO approximation is presented in the middle panel of Fig. 5. The slightly negative gap is due to the crossing the conduction band along the k - T symmetry direction. The optical gap is ~ 0.22 eV. The opening of the gap in $\text{Sr}_2\text{CrOsO}_6$ is not such as to produce a Mott insulator (it is a band insulator), but rather in the mold of

a “energy gap correction” to the GGA. To address the reported insulating character in $\text{Sr}_2\text{CrOsO}_6$ (versus the low DOS semimetal result obtained above), we applied intra-atomic Coulomb repulsion U on the Os ion using the LSDA+SO+OP method ($U_{\text{eff}} = U - J = 0$ eV). An insulating phase is obtained in the OP correction (see lower panel in Fig. 5).

4. XMCD spectra

4.1. W, Re, and Os $L_{2,3}$ XMCD spectra

Figure 7 shows the calculated XAS and XMCD spectra at the Re (upper panel) and Os (lower panel) $L_{2,3}$ edges in $\text{Sr}_2\text{CrReO}_6$ and $\text{Sr}_2\text{CrOsO}_6$ oxides, respectively, together with the experimental spectra. Figure 8 shows the calculated XAS and XMCD spectra at the W $L_{2,3}$ edges in Ca_2CrWO_6 (upper panel) and Sr_2CrW_6 (lower panel) oxides together with the experimental spectra. The Re, Os, and W L_3 XAS spectra ($2p_{3/2} \rightarrow 5d_{3/2,5/2}$ transitions) for these oxides have a strong resemblance to each other in a double peak structure. The energy splitting of these peaks is generally ascribed to the crystal field splitting of d orbitals into t_{2g} and e_g states [71]. The Re, Os, and W L_2 x-ray absorption spectra also have a double peak structure. Theory correctly reproduces the energy position and relative behavior of intensity in the L_3 and L_2 XASs.

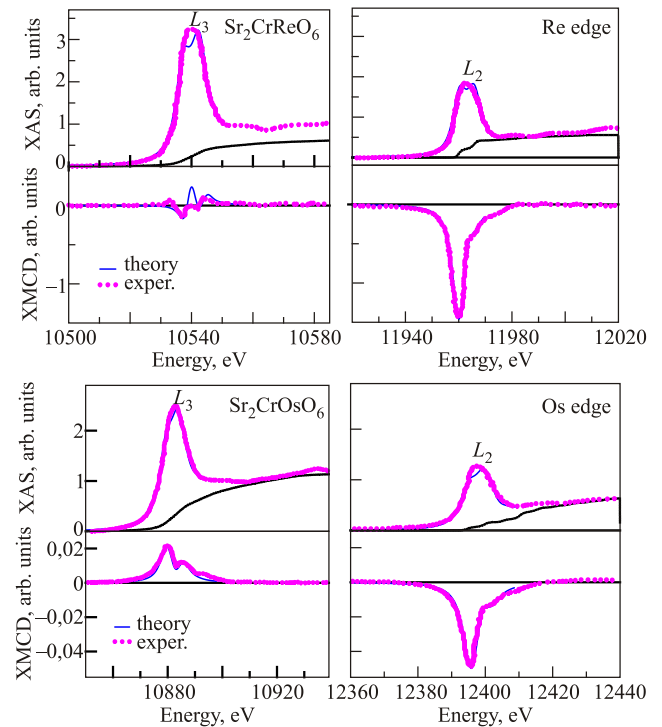


Fig. 7. (Color online) Upper panel: the experimental x-ray absorption spectra and XMCD spectra [72] (open circles) at the Re $L_{2,3}$ edges in $\text{Sr}_2\text{CrReO}_6$ compared with the theoretically calculated ones. Lower panel: the experimental x-ray absorption spectra and XMCD spectra [7] (open circles) at the Os $L_{2,3}$ edges in $\text{Sr}_2\text{CrOsO}_6$ compared with the theoretically calculated ones.

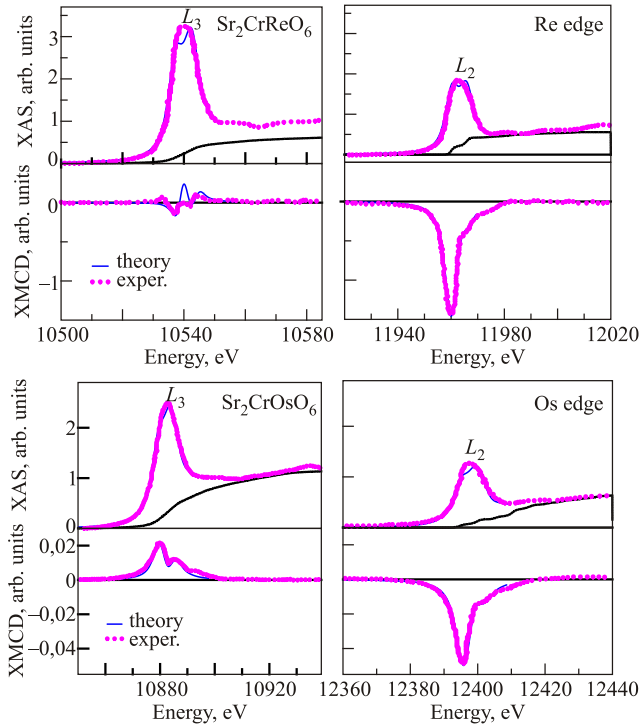


Fig. 8. (Color online) The experimental x-ray absorption spectra and XMCD spectra [20] (open circles) at the W $L_{2,3}$ edges in Ca_2CrWO_6 (upper panel) and Sr_2CrWO_6 (lower panel) compared with the theoretically calculated ones.

The experimentally measured dichroic L_2 line consists of a simple asymmetric negative peak with a high-energy shoulder in all the oxides under consideration. However, the XMCD spectra at the L_3 edge are significantly different from each other for different compounds. The Re L_3 XMCD spectrum in Sr_2CrReO_6 has a four peak structure: two positive (high and low energy) and two negative peaks. The negative peaks appear in between the two positive peaks. The dichroism at the Os L_3 edge in Sr_2CrOsO_6 has only two positive peaks (Fig. 7). The W L_3 XMCD spectra in Ca_2CrWO_6 and Sr_2CrWO_6 have four peak structures but with opposite sign: the highest low-energy peak is negative in Ca_2CrWO_6 and positive in Sr_2CrWO_6 . The dichroism at the L_3 edge is significantly smaller than at the L_2 edge in all four compounds.

A qualitative explanation of the XMCD spectra shape is provided by the analysis of the corresponding selection rules, orbital character and occupation numbers of individual $5d$ orbitals. Table 1 presents the dipole allowed transitions for x-ray absorption spectra at the L_3 and L_2 edges for left ($\lambda = +1$) and right ($\lambda = -1$) polarized x rays [73].

To go further, we need to discuss the character of the $5d$ empty DOS. From our band structure calculations we found that the Re $5d_{3/2}$ states with $m_j = -3/2$ and $-1/2$ are occupied in the Sr_2CrReO_6 oxides. For the $5d_{5/2}$ states the $m_j = 5/2$, and $3/2$ states are occupied. Therefore, for the Re L_2 XMCD spectrum the dipole allowed transitions

Table 1. The dipole allowed transitions from core $2p_{1/2,3/2}$ levels to unoccupied $5d_{3/2,5/2}$ valence states for left ($\lambda = +1$) and right ($\lambda = -1$) polarized x rays [73]

Edge	$\lambda = +1$	$\lambda = -1$
L_3 $2p_{3/2} \rightarrow 5d_{5/2}$	$-3/2 \rightarrow -1/2$	$-3/2 \rightarrow -5/2$
	$-1/2 \rightarrow +1/2$	$-1/2 \rightarrow -3/2$
	$+1/2 \rightarrow +3/2$	$+1/2 \rightarrow -1/2$
	$+3/2 \rightarrow +5/2$	$+3/2 \rightarrow +1/2$
L_3 $2p_{3/2} \rightarrow 5d_{3/2}$	$-3/2 \rightarrow -1/2$	$-1/2 \rightarrow -3/2$
	$-1/2 \rightarrow +1/2$	$+1/2 \rightarrow -1/2$
	$+1/2 \rightarrow +3/2$	$+3/2 \rightarrow +1/2$
L_2 $2p_{1/2} \rightarrow 5d_{3/2}$	$-1/2 \rightarrow +1/2$	$-1/2 \rightarrow -3/2$
	$+1/2 \rightarrow +3/2$	$+1/2 \rightarrow -1/2$

are only $-1/2 \rightarrow +1/2$ and $+1/2 \rightarrow +3/2$ for $\lambda = +1$ (Table 1). The $-1/2 \rightarrow -3/2$ and $+1/2 \rightarrow -1/2$ transitions are forbidden for $\lambda = -1$ because the $5d_{3/2}$ states with $m_j = -3/2$ and $-1/2$ are occupied. Thus the XMCD spectrum of Re at the L_2 edge ($I = \mu^- - \mu^+$) can be roughly approximated by the following sum of m_j -projected partial densities of states: $-(N_{1/2}^{3/2} + N_{3/2}^{3/2})$. Here we use the notation $N_{m_j}^j$ for the density of states with the total momentum j and its projection m_j . As a result, the shape of the Re L_2 XMCD spectrum contains an asymmetric negative peak.

A rather different situation occurs in the case of the L_3 XMCD spectrum. Analyzing the dipole selection rules and the character of the $5d_{5/2}$ empty states we can show that the XMCD spectrum of Re at the L_3 edge can be roughly approximated by the following sum of m_j -projected partial densities of states: $(N_{-5/2}^{5/2} + N_{-3/2}^{5/2}) - N_{3/2}^{3/2}$ [73]. From this expression one would expect a more complex structure for the XMCD spectra at the L_3 edge. The energy positions and peak intensities and even the number of peaks are very sensitive to the relative energy positions and intensities of the partial $5d_{3/2}$ and $5d_{5/2}$ DOSs as well as the occupation numbers of the $5d_{3/2}$ and $5d_{5/2}$ states. It determines a wide difference in the shape and relative intensities of the Re, Os, and W XMCD spectra at the L_3 edge. Theory relatively well describes the dichroism at the $L_{2,3}$ edges in the oxides under consideration.

4.2. Cr $L_{2,3}$ XMCD spectra

In complex transition metal ionic compounds such as Sr_2CrReO_6 , the XAS and XMCD spectra at the $L_{2,3}$ absorption edges can be used as fingerprints of the ground state. Figure 9 (upper panel) displays the experimentally measured Cr $L_{2,3}$ absorption spectra of Sr_2CrReO_6 [72]. The Cr L_3 x-ray absorption spectrum exhibits a doublet structure at the white line position (peaks a and b) and a weak high-energy shoulder c . The Cr L_2 XAS has a similar structure with double peaks d and e and a shoulder f . Authors of Ref. 72 interpreted the double peak structures of Cr $L_{2,3}$ XASs as the signature of the crystal field split-

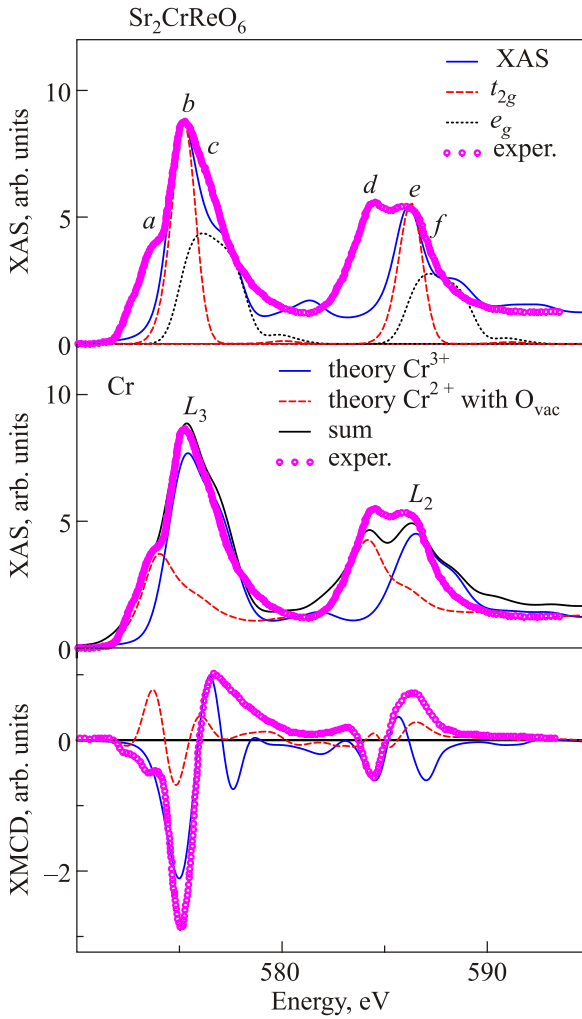


Fig. 9. (Color online) Upper panel: the experimental x-ray absorption spectra (open magenta circles) at the Cr $L_{2,3}$ edges in $\text{Sr}_2\text{CrReO}_6$ [72] compared with the theoretically calculated t_{2g} and e_g partial DOSs (dashed red and dotted black lines, respectively); middle panel: the experimental XAS spectra (open magenta circles) at the Cr $L_{2,3}$ edges in $\text{Sr}_2\text{CrReO}_6$ [72] compared with the theoretically calculated ones (full black curve) with an oxygen vacancy (the contributions from the Cr^{3+} and Cr^{2+} ions are presented by full blue and dashed red curves, respectively); lower panel: the experimental XMCD spectra (open magenta circles) at the Cr $L_{2,3}$ edges in $\text{Sr}_2\text{CrReO}_6$ [72] compared with the theoretically calculated ones for Cr^{3+} and Cr^{2+} ions (full blue blue and dashed red curves, respectively) in $\text{Sr}_2\text{CrReO}_6$ with an oxygen vacancy.

ting of the $3d$ band into t_{2g} and e_g states. Peak a (d) was associated with t_{2g} states and peak b (e) with e_g states in the L_3 (L_2) XAS. This assertion by Hauser *et al.* [72] is not correct.

We found that the GGA (as well as LSDA) produces a half-metallic ground state self-consistent solution in $\text{Sr}_2\text{CrReO}_6$ with trivalent Cr^{3+} ions. Figure 9 (upper panel) shows the experimentally measured Cr $L_{2,3}$ XAS together with the theoretically calculated Cr $3d$ partial DOSs

broaden to take into account the apparative resolution and finite lifetime of core $L_{2,3}$ levels. Although, the energy splitting between a and b peaks in the L_3 XAS is close to the crystal field splitting of the $3d$ band, the t_{2g} states are much narrower than the e_g states (see upper panel of Fig. 10). Therefore, the peak b is derived mostly from the t_{2g} states with some additional contribution from the e_g states, the high-energy shoulder c is due to the e_g states (upper panel of Fig. 9). We can conclude that the complex fine structure of the Cr $L_{2,3}$ XAS is not compatible with a pure a Cr^{3+} valency state. The calculations for the ideal crystal structure with Cr^{3+} ground-state solution provide the x-ray absorption intensity only at the major peak b and high-energy shoulder c and do not reproduce the low-energy shoulder (peak a) as well as low-energy peak d at the L_2 edge.

The interpretation demands mixed valent states in $\text{Sr}_2\text{CrReO}_6$. It is not clear yet the nature of Cr mixed valency in $\text{Sr}_2\text{CrReO}_6$. One of the possible reason of mixed valent states in $\text{Sr}_2\text{CrReO}_6$ is lattice defects. We investigated the influence of oxygen deficiency. We created an oxygen vacancy in a double super-cell of $\text{Sr}_2\text{CrReO}_6$ ($\text{Sr}_2\text{CrReO}_{6-\delta}$, $\delta = 0.5$) in the first neighborhood of the second Cr_2 atom at the 1.955 Å distance. The corresponding distance between the Cr_1 ion and oxygen vacancy is equal to 4.3655 Å. To investigate possible lattice distortion due to the oxygen vacancy we optimized the position of

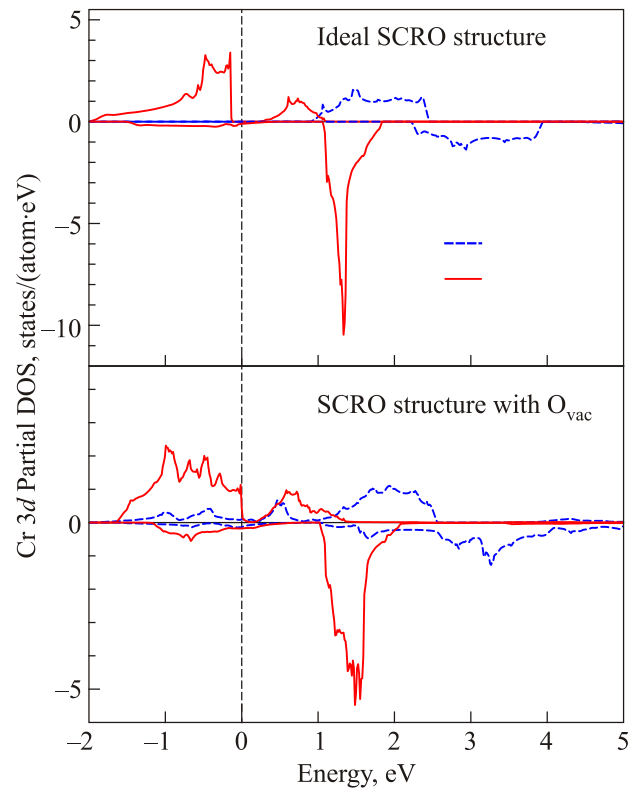


Fig. 10. (Color online) Upper panel: Cr $3d$ partial DOSs for the ideal $\text{Sr}_2\text{CrReO}_6$ (SCRO) structure; lower panels: Cr $3d$ partial DOSs for the $\text{Sr}_2\text{CrReO}_6$ with an oxygen vacancy.

neighbor atoms around the oxygen vacancy with fixed positions of the other atoms using the VASP-SGGA method [44,74,75]. We found that the existence of the oxygen vacancy shifts the valency of the nearest Cr ion towards $2+$. Self-consistent calculations produce the valency equal to $2.9+$ and $2.4+$ at the Cr_1 and Cr_2 sites, respectively. The oxygen vacancy also destroys the half-metallicity in Sr_2CrReO_6 (see lower panel of Fig. 10).

As can be seen from Fig. 9 (middle panel) the x-ray absorption from the Cr_2^{2+} atoms with the oxygen vacancy (red dashed line) contributes to the low-energy peak *a* of the L_3 x-ray absorption and peak *d* at the L_2 edge. The relative intensity of the *a* and *b* peaks depends on the relative concentration of the Cr_1 and Cr_2 ions in Sr_2CrReO_6 , in another words, the concentration of defects such as an oxygen vacancy. We found that the best agreement between the calculations and experimental data corresponds to a linear combination of 69% Cr^{3+} and 31% Cr^{2+} ions. A similar situation was observed in the Sr_2FeMoO_6 perovskite where a mixed valence state at the Fe site was occurred with proportion of 66% Fe^{2+} and 34% Fe^{3+} states [76].

Figure 9 (lower panel) presents the experimental XMCD spectra at the Cr $L_{2,3}$ edges in Sr_2CrReO_6 [72] compared with the theoretically calculated ones for Cr^{3+} and Cr^{2+} ions in Sr_2CrReO_6 . The XMCD spectrum at the Cr L_3 edge possesses a strong negative peak at around 577.3 eV and a high-energy positive shoulder. The Cr^{2+} ions contribute to the lower energy fine structure at the L_3 edge around 576 eV and to the positive peak at the L_2 edge at 587 eV. The major negative peak of the L_3 XMCD at 577.3 eV and the negative peak at 585.5 eV of the L_2 XMCD are mostly due to the Cr^{3+} ions.

Hauser *et al.* [77] recently showed that the electrical resistivity of Sr_2CrReO_6 films appears to be strongly modulated by oxygen partial pressure within a narrow window of oxygen partial pressures ($P_{O_2} = 25$ to $28.75 \mu\text{Torr}$), likely due to changing levels of oxygen vacancies created by the growth environment. It would be highly desired to measure the XMCD spectra at the Cr $L_{2,3}$ edges with the oxygen partial pressure.

Figure 11 (upper panel) presents the experimental x-ray absorption spectra [19] (open circles) at the Cr $L_{2,3}$ edges in Sr_2CrWO_6 compared with the theoretically calculated ones. The complex fine structure of the Cr $L_{2,3}$ XAS in Sr_2CrWO_6 is not compatible with a pure Cr^{3+} valency state. The calculations for the ideal crystal structure with a Cr^{3+} ground-state solution provide the x-ray absorption intensity only at the major peak and high-energy shoulder and do not reproduce the low-energy shoulder as well as the low-energy peak at the L_2 edge. The interpretation demands mixed valent states in Sr_2CrWO_6 . The x-ray absorption from the Cr_2^{2+} atoms with an oxygen vacancy (red line) contributes to the low-energy peaks of L_3 and L_2 x-ray absorption edges.

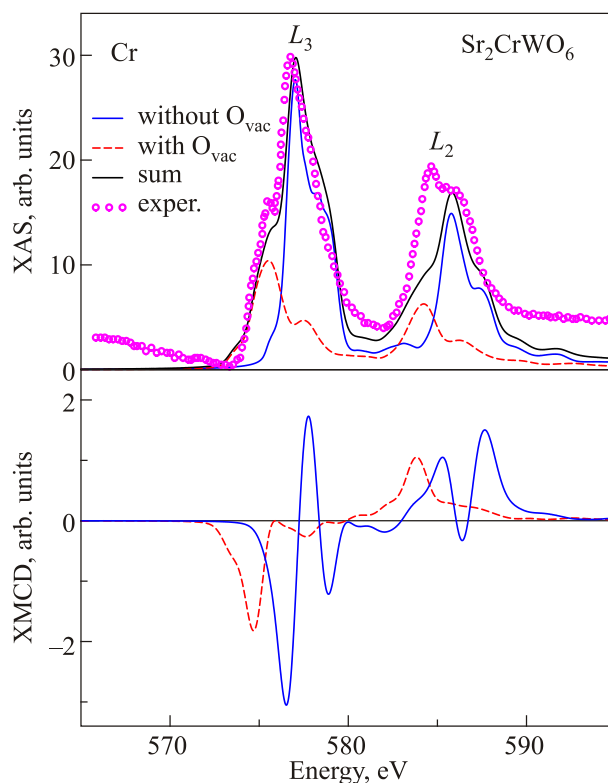


Fig. 11. (Color online) Upper panel: the experimental XAS spectra (open magenta circles) at the Cr $L_{2,3}$ edges in Sr_2CrWO_6 [19] compared with the theoretically calculated ones (full black curve) with an oxygen vacancy (the contributions from the Cr^{3+} and Cr^{2+} ions are presented by full blue and dashed red curves, respectively); lower panel: the theoretically calculated XMCD spectra for Cr^{3+} and Cr^{2+} ions (full blue and dashed red curves, respectively) in Sr_2CrReO_6 with an oxygen vacancy.

4.3. Cr and O K XAS and XMCD spectra in Sr_2CrWO_6

The XAS and XMCD spectra in metals and alloys at the K edge when the $1s$ core electrons are excited to p states through the dipolar transitions are quite important. They are sensitive to the electronic states at neighboring sites because of the delocalized nature of valence p states.

The XAS at the Cr K edge in the Sr_2CrWO_6 samples were measured by Chan *et al.* [78]. Figure 12 shows calculated Cr K XAS and XMCD spectra together with the experimental ones [78]. The Cr K XAS spectrum is quite structured, showing well defined features. The main traits of this spectrum are a strong resonance at the threshold, some low-energy pre-peak structures and a shoulder above the threshold. The major peak at 6006 eV and high-energy shoulder are ascribed to dipolar $1s \rightarrow 4p$ transitions whose shape and intensity are related to local geometrical characteristics such as the scattering power of the Cr atom. Pre-peak features are also ascribed to the dipolar transitions in our calculations. We found that the Cr K XAS spectra for the Cr^{3+} state (blue full curve in upper panel of Fig. 12) and Cr^{2+} states which appear with an oxygen vacancy (red dashed curve) have almost the same shapes.

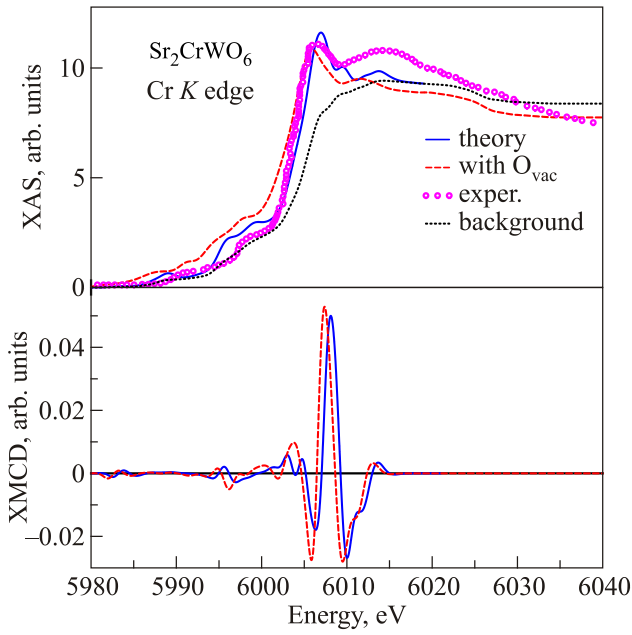


Fig. 12. (Color online) The experimentally measured x-ray absorption spectrum at the Cr *K* edge in Sr₂CrWO₆ [78] compared with the theoretically calculated ones.

The lower panel of Fig. 12 shows the Cr *K* theoretically calculated XMCD spectra. The shape and relative intensities of the fine structures for Cr³⁺ and Cr²⁺ solutions are also very similar. The experimental measurements of the Cr *K* XMCD spectra is highly desired.

Figure 13 presents the experimental O *K* x-ray absorption spectrum (open circles in upper panel) in Sr₂CrWO₆ [78] compared with the theoretically calculated ones. The O *K* XAS spectrum of Sr₂CrWO₆ oxide is spreaded up to 25 eV above the threshold and quite structured, showing well defined features. The main features of these spectra are a strong resonance at the threshold and some high-energy peaks followed after a low minimum. The spectral features just above the threshold are attributed mainly to the oxygen 2*p* empty orbitals hybridized with the W 5*d* and Cr 3*d* orbitals. The fine structures situated between 5 and 15 eV are due to the O 2*p* orbitals hybridized with the Cr 4*s* and 4*p* and W 6*s* and 6*p* orbitals.

The dichroism at the O *K* edge (lower panel of Fig. 13) is significant only for the 2*p* states which strongly hybridize with the W 5*d* and Cr 3*d* states at the 0 to 4 eV energy interval. The spectral XMCD features between 5 and 15 eV which are due to the O 2*p* orbitals hybridized with the W and Cr *s* and *p* orbitals are extremely small.

4.4. Magnetic moments

In magnets, the spin M_s and orbital M_l magnetic moments are basic quantities and their separate determination is therefore important. Methods of their experimental determination include traditional gyromagnetic ratio measurements [79], magnetic form factor measurements using

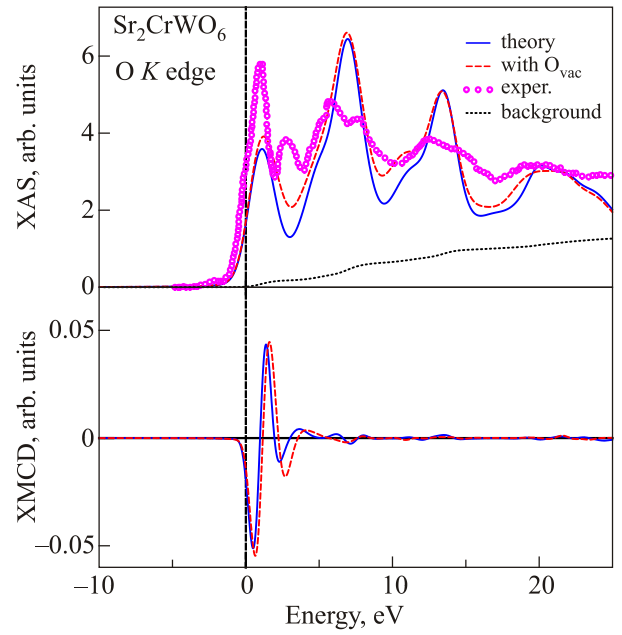


Fig. 13. (Color online) The experimentally measured x-ray absorption spectrum at the O *K* edge in Sr₂CrWO₆ [78] compared with the theoretically calculated ones for ideal structure (blue full curves) and with an oxygen vacancy (red dashed curves).

neutron scattering [80], and magnetic x-ray scattering [81]. In addition to these, the x-ray magnetic circular dichroism combined with several sum rules [32,33] has attracted much attention as a method of site- and symmetry-selective determination of M_s and M_l . Table 2 presents the comparison between calculated and experimental magnetic moments at the W, Re, and Os sites in Sr₂CrWO₆, Sr₂CrReO₆, and Sr₂CrOsO₆, respectively. Table 3 presents the comparison between calculated and experimental magnetic moments at the Cr site in Sr₂CrWO₆, Sr₂CrReO₆, and Sr₂CrOsO₆.

Table 2. The theoretically calculated and experimentally measured spin M_s and orbital M_l magnetic moments (in μ_B) at the W, Re, and Os sites in Sr₂CrWO₆, Sr₂CrReO₆, and Sr₂CrOsO₆, respectively

Method	W		Re		Os	
	M_s	M_l	M_s	M_l	M_s	M_l
GGA+SO	-0.332	0.085	-1.087	0.286	-1.434	0.104
Sum rules	-0.295	0.068	-1.063	0.255	-1.236	0.103
Exp. [20] (XMCD)	-0.33	0.12	-	-	-	-
Exp. [21] (XMCD)	-	-	-0.68	0.25	-	-
Theory [14]	-	-	-	-	-1.312	0.173
Theory [17]	-0.31	0.10	-0.85	0.18	-	-
Theory [7]	-	-	-	-	-1.214	0.122
Theory [22]	-	-	-0.78	0.20	-	-
Theory [10]	-0.30	0.07	-0.87	0.17	-1.32	0.11
Theory [82]	-	-	-1.31	0.69	-	-
Theory [23]	-0.27	0.10	-	-	-	-

Table 3. The theoretically calculated and experimentally measured spin M_s and orbital M_l magnetic moments (in μ_B) at the Cr site in Sr_2CrWO_6 , Sr_2CrReO_6 , and Sr_2CrOsO_6

Method	Sr_2CrWO_6		Sr_2CrReO_6		Sr_2CrOsO_6	
	M_s	M_l	M_s	M_l	M_s	M_l
GGA+SO	2.289	-0.030	2.399	-0.038	2.289	-0.031
Sum rules	1.916	-0.032	2.016	-0.048	1.939	-0.024
Theory [14]	-	-	-	-	2.194	0.142
Theory [17]	-	-	2.02	-0.29	-	-
Theory [22]	-	-	2.02	-0.029	-	-
Theory [10]	2.15	-0.02	2.17	-0.03	2.21	-0.02
Theory [82]	-	-	2.52	-0.04	-	-
Theory [23]	2.20	-0.017	-	-	-	-
Theory [7]	-	-	-	-	2.216	-0.024

The Cr, W, Re, and Os spin and orbital moments are antiparallel in the oxides under consideration, in accordance with the Hund's third rule. The GGA W spin moment of $-0.332 \mu_B$ as well as orbital moment $0.085 \mu_B$ are in good agreement with the previous calculations [10,17,23] of Sr_2CrWO_6 . However, our Re spin magnetic moment in Sr_2CrReO_6 is slightly larger than the results of Refs. 10, 17, 22, as well as the experimental data [21], but still smaller than the data of Wang *et al.* [82]. Our spin and orbital magnetic moments at the Cr site are in reasonably good agreement with the results obtained by other authors (Table 3). The results from different calculations may vary somewhat since the calculated moments depend on the details of the calculations and especially on the sizes of the muffin-tin spheres which usually differ from each other for different calculations.

Tables 2 and 3 also present the Cr, W, Re, and Os magnetic moments obtained from the XMCD experiments. In these experiments spin and orbital magnetic moments obtained by using the sum rules [32,33] which relate the integrated signals over the spin-orbit split core edges of the circular dichroism to ground-state orbital and spin magnetic moments. The XMCD sum rules are derived within an ionic model using a number of approximations [83]. It is well known that the application of the sum rules sometimes results in an error up to 50% [36]. However, we found relatively good agreement between the theoretically calculated magnetic moment and derived from the experimental XAS and XMCD spectra, especially in the case of the spin magnetic moment at the W and Os sites, as well as the orbital magnetic moment at the Re site (Table 2).

To investigate the possible error of the sum rules we compare the spin and orbital moments obtained from the theoretically calculated XAS and XMCD spectra through the sum rules with directly calculated GGA values in order to avoid additional experimental problems. The sum rules [Eqs. (3) and (4)] reproduce the spin magnetic moments

within 11%, 2%, and 13% and the orbital moments within 20%, 11% and 1% at the W, Re, and Os sites, respectively (Table 2). The spin magnetic moments at the Cr site are reproduced within 16%, 16%, and 15% and the orbital moments within 7%, 20% and 22% in Sr_2CrWO_6 , Sr_2CrReO_6 , and Sr_2CrOsO_6 , respectively (Table 3).

Finally, our calculations produce induced spin and orbital magnetic moments at the oxygen site in Sr_2CrWO_6 of about 0.011 and 0.002 μ_B , respectively. Two nonequivalent oxygen atoms in Sr_2CrReO_6 have $M_s^{O1} = -0.017 \mu_B$, $M_s^{O2} = -0.031 \mu_B$, $M_l^{O1} = 0.022 \mu_B$, and $M_l^{O2} = -0.005 \mu_B$. The magnetic moments in Sr_2CrOsO_6 at the oxygen site are equal to $M_s = -0.084 \mu_B$ and $M_l = -0.005 \mu_B$.

5. Conclusions

A systematic electronic structure study of $A_2CrB'O_6$ ($A = Ca, Sr; B' = W, Re, \text{ and } Os$) has been performed by employing the local spin density approximation (LSDA) as well as the GGA and GGA+*U* methods using the fully relativistic spin-polarized Dirac linear muffin-tin orbital band-structure method. We investigated the effects of the subtle interplay among the spin-orbit coupling, electron correlations, and lattice distortion on the electronic structure of the double perovskites.

First principles calculations predict that Sr_2CrOsO_6 is (before considering SOC) actually a ferrimagnetic semimetal with precisely compensating spin moments, or a *spin-asymmetric compensated semimetallic ferrimagnet* in which the electrons and holes are each fully polarized and have opposite spin directions, in spite of a zero net moment and hence no macroscopic magnetic field. The SOC degrades this by giving a nonzero total moment, but the band structure is little changed. Therefore, the observed saturation moment of ferrimagnetic Sr_2CrOsO_6 is entirely due to spin-orbit coupling.

The x-ray absorption spectra and x-ray magnetic circular dichroism at the Cr, W, Re, and Os $L_{2,3}$ edges in $A_2CrB'O_6$ ($A = Ca, Sr; B' = W, Re, \text{ and } Os$) oxides and Cr and O *K* edges in Sr_2CrW_6 were investigated theoretically in the frame of the fully relativistic LMTO method. The theory relatively well describes the shape and relative intensities of the x-ray absorption and XMCD spectra in the double oxides. The experimentally measured dichroic W, Re, and Os L_2 lines consist of an intensive asymmetric negative peak in all the compounds. The XMCD at the L_3 edges have more complex structure with two (in Sr_2CrOsO_6) or four peaks (in other compounds). A qualitative explanation of the $L_{2,3}$ XMCD spectra is provided by the analysis of the corresponding selection rules, orbital character and occupation numbers of individual 5*d* orbitals. The XMCD spectra at the Re L_2 edge can be roughly approximated by the following sum of m_j -projected partial densities of

states: $-(N_{1/2}^{3/2} + N_{3/2}^{3/2})$. As a result, the shape of the Re (as well as W and Os) L_2 XMCD spectra contains an asymmetric negative peak. The L_3 XMCD spectra possess more complex structures. The energy position and peak intensities and even the number of the peaks of the L_3 XMCD spectra are very sensitive to the relative energy positions and intensities of the partial $5d_{3/2}$ and $5d_{5/2}$ DOSs as well as the occupation numbers of the $5d_{3/2}$ and $5d_{5/2}$ states. Theory relatively well describes the dichroism at the $L_{2,3}$ edges in the oxides under consideration.

The complex fine structure of the Cr $L_{2,3}$ XAS in Sr_2CrWO_6 and $\text{Sr}_2\text{CrReO}_6$ is not compatible with a pure Cr^{3+} valency state. The calculations for the ideal crystal structure with a Cr^{3+} ground state solution provide the x-ray absorption intensity only at the major peak and high energy shoulder and do not reproduce the low-energy shoulder as well as the low-energy peak at the L_2 edge. The interpretation demands mixed valent states in Sr_2CrWO_6 and $\text{Sr}_2\text{CrReO}_6$. The x-ray absorption from the Cr_2^{2+} atoms with an oxygen vacancy contributes to the low-energy peaks of the L_3 and L_2 x-ray absorption edges. We can conclude that possible oxygen vacancies lead to a mixed valency at the Cr site, double peak structure at the Cr $L_{2,3}$ edges and reduce the saturation magnetization in Sr_2CrWO_6 and $\text{Sr}_2\text{CrReO}_6$.

The dichroism at the O K edge in Sr_2CrWO_6 is significant only for the $2p$ states which strongly hybridize with the W $5d$ and Cr $3d$ states at the 0 to 4 eV energy interval. The spectral XMCD features between the 5 and 15 eV which are due to the O $2p$ orbitals hybridized with the W and Cr s and p orbitals are extremely small.

Acknowledgments

We are thankful to Dr. A.N. Yaresko for helpful discussions. This work was supported by Science and Technology Center in Ukraine STCU, Project No. 6255.

1. K.I. Kobayashi, T. Kimura, H. Sawada, K. Terakura, and Y. Tokura, *Nature* **395**, 677 (1998).
2. H. Kato, T. Okuda, Y. Okimoto, Y. Tomioka, K. Oikawa, T. Kamiyama, and Y. Tokura, *Phys. Rev. B* **69**, 184412 (2004).
3. J.M.D. Coey, *Adv. Phys.* **48**, 167 (1999).
4. D. Serrate, J.M.D. Teresa, and M.R. Ibarra, *J. Phys.: Condens. Matter* **19**, 023201 (2007).
5. S.A. Wolf, D.D. Awschalom, R.A. Buhrman, J.M. Daughton, S. von Molnar, M.L. Roukes, A.Y. Chtchelkanova, and D.M. Treger, *Science* **294**, 1488 (2001).
6. A.W. Sleight, J. Longo, and R. Ward, *Inorg. Chem.* **1**, 245 (1962).
7. Y. Kronenberger, K. Mogare, M. Reehuis, M. Tovar, M. Jansen, G. Vaitheeswaran, V. Kanchana, F. Bultmark, A. Delin, F. Wilhelm, A. Rogalev, A. Winkler, and L. Alff, *Phys. Rev. B* **75**, 020404(R) (2007).

8. J.B. Philipp, P. Majewski, L. Alff, A. Erb, R. Gross, T. Graf, M.S. Brandt, J. Simon, T. Walther, W. Mader, D. Topwal, and D.D. Sarma, *Phys. Rev. B* **68**, 144431 (2003).
9. H. Kato, T. Okuda, Y. Okimoto, Y. Tomioka, K. Oikawa, T. Kamiyama, and Y. Tokura, *Phys. Rev. B* **65**, 144404 (2002).
10. H. Das, M.D. Raychaudhury, and T. Saha-Dasgupta, *Appl. Phys. Lett.* **92**, 201912 (2008).
11. X. Chen, D. Parker, K.P. Ong, M.-H. Du, and D.J. Singh, *Appl. Phys. Lett.* **102**, 102403 (2013).
12. H. Das, P. Sanyal, T. Saha-Dasgupta, and D.D. Sarma, *Phys. Rev. B* **83**, 104418 (2011).
13. T.K. Mandal, C. Felser, M. Greenblatt, and J. Kubler, *Phys. Rev. B* **78**, 134431 (2008).
14. K.-W. Lee and W.E. Pickett, *Phys. Rev. B* **77**, 115101 (2008).
15. H. Kato, T. Okuda, Y. Okimoto, Y. Tomioka, Y. Takenoya, A. Ohkubo, M. Kawasaki, and Y. Tokura, *Appl. Phys. Lett.* **81**, 328 (2002).
16. C.Q. Tang, Y. Zhang, and J. Dai, *Solid State Commun.* **133**, 219 (2005).
17. G. Vaitheeswaran and V.K.A. Delin, *Appl. Phys. Lett.* **86**, 032513 (2005).
18. A.J. Hauser, J.R. Soliz, M. Dixit, R.E.A. Williams, M.A. Susner, B. Peters, L.M. Mier, T.L. Gustafson, M.D. Sumption, H.L. Fraser, P.M. Woodward, and F.Y. Yang, *Phys. Rev. B* **85**, 161201(R) (2012).
19. T.S. Chan, R.S. Liu, and C.Y. Huang, *Inter. J. Mod. Phys. B* **19**, 537 (2005).
20. P. Majewski, S. Geprgs, A. Boger, M. Opel, A. Erb, R. Gross, G. Vaitheeswaran, V. Kanchana, A. Delin, F. Wilhelm, A. Rogalev, and L. Alff, *Phys. Rev. B* **72**, 132402 (2005).
21. P. Majewski, S. Geprgs, O. Sanganas, M. Opel, R. Gross, F. Wilhelm, A. Rogalev, and L. Alff, *Appl. Phys. Lett.* **87**, 202503 (2005).
22. G. Vaitheeswaran, V. Kanchana, M. Alouani, and A. Delin, *Europhys. Lett.* **84**, 47005 (2008).
23. H.-T. Jeng and G.Y. Guo, *Phys. Rev. B* **67**, 094438 (2003).
24. V.I. Anisimov, J. Zaanen, and O.K. Andersen, *Phys. Rev. B* **44**, 943 (1991).
25. A.M. Glazer, *Acta Crystallogr. B* **28**, 3384 (1972).
26. J.M. Michalik, J.M.D. Teresa, J. Blasco, P.A. Algarabel, M.R. Ibarra, C. Kapusta, and U. Zeitler, *J. Phys.: Condens. Matter* **19**, 506206 (2007).
27. G.Y. Guo, H. Ebert, W.M. Temmerman, and P.J. Durham, *Phys. Rev. B* **50**, 3861 (1994).
28. V.N. Antonov, A.I. Bagljuk, A.Y. Perlov, V.V. Nemoskhalenko, V.N. Antonov, O.K. Andersen, and O. Jepsen, *Fiz. Nizk. Temp.* **19**, 689 (1993) [*Low Temp. Phys.* **19**, 494 (1993)].
29. V. Antonov, B. Harmon, and A. Yaresko, *Electronic Structure and Magneto-Optical Properties of Solids*, Kluwer, Dordrecht (2004).
30. E. Arola, M. Horne, P. Strange, H. Winter, Z. Szotek, and W.M. Temmerman, *Phys. Rev. B* **70**, 235127 (2004).
31. G. van der Laan and B.T. Thole, *Phys. Rev. B* **38**, 3158 (1988).

32. B.T. Thole, P. Carra, F. Sette, and G. van der Laan, *Phys. Rev. Lett.* **68**, 1943 (1992).
33. P. Carra, B.T. Thole, M. Altarelli, and X. Wang, *Phys. Rev. Lett.* **70**, 694 (1993).
34. G. van der Laan and B.T. Thole, *Phys. Rev. B* **53**, 14458 (1996).
35. V.N. Antonov, B.N. Harmon, and A.N. Yaresko, *Phys. Rev. B* **63**, 205112 (2001).
36. V.N. Antonov, O. Jepsen, A.N. Yaresko, and A.P. Shpak, *J. Appl. Phys.* **100**, 043711 (2006).
37. V.N. Antonov, M. Galli, F. Marabelli, A.A. Yaresko, A.Ya. Perlov, and E. Bauer, *Phys. Rev. B* **62**, 1742 (2000).
38. O.K. Andersen, *Phys. Rev. B* **12**, 3060 (1975).
39. V.V. Nemoshkalenko, A.E. Krasovskii, V.N. Antonov, V.N. Antonov, U. Fleck, H. Wonn, and P. Ziesche, *Phys. Status Solidi B* **120**, 283 (1983).
40. V.N. Antonov, A.Y. Perlov, A.P. Shpak, and A.N. Yaresko, *J. Magn. Magn. Mater.* **146**, 205 (1995).
41. S. Park, H.J. Ryu, S.B. Kim, B.W. Lee, and C.S. Kim, *Physica B* **345**, 99 (2004).
42. J. Perdew and Y. Wang, *Phys. Rev. B* **45**, 13244 (1992).
43. J.P. Perdew, K. Burke, and M. Ernzerhof, *Phys. Rev. Lett.* **77**, 3865 (1996).
44. J.P. Perdew, K. Burke, and M. Ernzerhof, *Phys. Rev. Lett.* **78**, 1396 (1997).
45. P.E. Blöchl, O. Jepsen, and O.K. Andersen, *Phys. Rev. B* **49**, 16223 (1994).
46. J.L. Campbell and T. Parr, *At. Data Nucl. Data Tables* **77**, 1 (2001).
47. J.P. Perdew and A. Zunger, *Phys. Rev. B* **23**, 5048 (1981).
48. L. Hedin, *Phys. Rev.* **139**, A 796 (1965).
49. W. Metzner and D. Vollhardt, *Phys. Rev. Lett.* **62**, 324 (1989).
50. T. Pruschke, M. Jarell, and J.K. Freericks, *Adv. Phys.* **44**, 187 (1995).
51. A. Georges, G. Kotliar, W. Krauth, and M.J. Rozenberg, *Rev. Mod. Phys.* **68**, 13 (1996).
52. A.N. Yaresko, V.N. Antonov, and P. Fulde, *Phys. Rev. B* **67**, 155103 (2003).
53. V.I. Anisimov and O. Gunnarsson, *Phys. Rev. B* **43**, 7570 (1991).
54. I.V. Solovyev, P.H. Dederichs, and V.I. Anisimov, *Phys. Rev. B* **50**, 16861 (1994).
55. P.H. Dederichs, S. Blügel, R. Zeller, and H. Akai, *Phys. Rev. Lett.* **53**, 2512 (1984).
56. W.E. Pickett, S.C. Erwin, and E.C. Ethridge, *Phys. Rev. B* **58**, 1201 (1998).
57. M. Cococcioni and S. de Gironcoli, *Phys. Rev. B* **71**, 035105 (2005).
58. K. Nakamura, R. Arita, Y. Yoshimoto, and S. Tsuneyuki, *Phys. Rev. B* **74**, 235113 (2006).
59. F. Aryasetiawan, M. Imada, A. Georges, G. Kotliar, S. Biermann, and A.I. Lichtenstein, *Phys. Rev. B* **70**, 195104 (2004).
60. I.V. Solovyev and M. Imada, *Phys. Rev. B* **71**, 045103 (2005).
61. V.P. Antropov, V.N. Antonov, L.V. Bekenov, A. Kutepov, and G. Kotliar, *Phys. Rev. B* **90**, 054404 (2014).
62. F. Aryasetiawan, K. Karlsson, O. Jepsen, and U. Schonberger, *Phys. Rev. B* **74**, 125106 (2006).
63. M.S.S. Brooks, *Physica B* **130**, 6 (1985).
64. O. Eriksson, M.S.S. Brooks, and B. Johansson, *Phys. Rev. B* **41**, 7311 (1990).
65. L. Severin, M.S.S. Brooks, and B. Johansson, *Phys. Rev. Lett.* **71**, 3214 (1993).
66. A. Mavromaras, L. Sandratskii, and J. Kübler, *Solid State Commun.* **106**, 115 (1998).
67. A.R. Mackintosh and O.K. Andersen, in: *Electrons at the Fermi Surface*, M. Springford (ed.), Cambridge University Press, Cambridge (1980), p. 149.
68. B.C. Jeon, C.H. Kim, S.J. Moon, W.S. Choi, H. Jeong, Y.S. Lee, J. Yu, C.J. Won, J.H. Jung, N. Hur, and T.W. Noh, *J. Phys.: Condens. Matter* **22**, 345602 (2010).
69. G. Vaitheeswaran, V. Kanchana, and A. Delin, *J. Phys.: Conf. Ser.* **29**, 50 (2006).
70. J. Wang, J. Meng, and Z. Wu, *J. Comput. Chem.* **32**, 3313 (2011).
71. F.M.F. Groot, *Physica B* **208–209**, 15 (1995).
72. A.J. Hauser, J.M. Lucy, M.W. Gaultois, M.R. Ball, J.R. Soliz, Y. Choi, O.D. Restrepo, W. Windl, J.W. Freeland, D. Haskel, P.M. Woodward, and F. Yang, *Phys. Rev. B* **89**, 180402(R) (2014).
73. V.N. Antonov, L.V. Bekenov, and A. Ernst, *Phys. Rev. B* **94**, 035122 (2016).
74. P.E. Blöchl, *Phys. Rev. B* **50**, 17953 (1994).
75. G. Kresse and J. Joubert, *Phys. Rev. B* **59**, 1758 (1999).
76. M. Besse, V. Cros, A. Barthelemy, H. Jaffres, J. Vogel, F. Petroff, A. Mirone, A. Tagliaferri, P. Bencok, P. Decorse, P. Berthet, Z. Szotek, W.M. Temmerman, S.S. Dhesi, N.B. Brookes, A. Rogalev, and A. Fert, *Europhys. Lett.* **60**, 608 (2002).
77. A.J. Hauser, J.M. Lucy, H.L. Wang, J.R. Soliz, A. Holcomb, P. Morris, P.M. Woodward, and F.Y. Yang, *Appl. Phys. Lett.* **102**, 032403 (2013).
78. T.S. Chan, R.S. Liu, G.Y. Guo, S.F. Hu, J.G. Lin, J.-F. Lee, L.-Y. Jang, C.-R. Chang, and C.Y. Huang, *Solid State Commun.* **131**, 531 (2004).
79. G.G. Scott, *J. Phys. Soc. Jpn.* **17**, 372 (1962).
80. W. Marshall and S.W. Lovsey, *Theory of Thermal Neutron Scattering*, Oxford University Press, Oxford (1971).
81. M. Blume, *J. Appl. Phys.* **57**, 3615 (1985).
82. J. Wang, N.N. Zu, Y. Wang, and Z.J. Wu, *J. Magn. Magn. Mater.* **339**, 163 (2013).
83. H. Ebert, *Rep. Prog. Phys.* **59**, 1665 (1996).